Observational validation of parameterized gravity waves from tropical convection in the Whole Atmosphere Community Climate Model (WACCM)

M. J. Alexander[1], C. C. Liu[2], J. Bacmeister[3], M. Bramberger[1], A. Hertzog[4], and J. H. Richter[3]

[1]NorthWest Research Associates, Boulder Office
[2]Texas A&M University, Corpus Christie
[3]National Center for Atmospheric Research
[4]Laboratoire de Meteorologie Dynamique

Key Points:

- WACCM subgrid-scale gravity wave and deep convection properties are validated using tropical observations.
- Optimal subgrid-scale convective fraction and heating depth parameters are found through the validation.
- Adding the missing stationary component of gravity waves above convection would likely improve QBO simulations.

Corresponding author: M. Joan Alexander, alexand@nwra.com

Abstract

Tropical gravity waves that are generated by convection are generally too small in scale and too high in frequency to be resolved in global climate models, yet their drag forces drive the important global-scale quasi-biennial oscillation (QBO) in the lower stratosphere, and models rely on parameterizations of gravity wave drag to simulate the QBO. We compare detailed properties of tropical parameterized gravity waves in the Whole Atmosphere Community Climate Model Version 6 (WACCM6) with gravity waves observed by long-duration super-pressure balloons, and also compare properties of parameterized convective latent heating with satellite data. Similarities and differences suggest that the WACCM6 parameterizations are excellent tools for representing tropical gravity waves, but the results also suggest detailed changes to the gravity wave parameterization tuning parameter assumptions that would bring the parameterized waves into much better agreement with observations. While WACCM6 currently includes only non-stationary gravity waves from convection, addition of the component that is stationary relative to convective rain cells is likely to improve the simulation of the QBO in the model. The suggested changes have the potential to alleviate common biases in simulated QBO circulations in models.

1 Introduction

Tropical gravity waves that drive the middle atmospheric circulations are primarily generated by tropical convection. Together with planetary-scale Kelvin waves, their breaking and dissipation in the stratosphere drives the descent of lower stratospheric zonal wind changes in the Quasi-Biennial Oscillation (QBO). Most global models seeking to represent the QBO include parameterizations of tropical gravity wave drag to approximate the necessary momentum forces (Butchart et al., 2018). The QBO is simulated within current climate prediction models only when these parameterizations are included. Tropical gravity wave parameterizations often require labor-intensive tuning of multiple parameters to achieve a reasonable QBO in models: The tuning parameters are unfortunately poorly constrained observationally, and the QBO circulation in the models tends to be highly sensitive to the parameter choices (Giorgetta, Manzini, Roeckner, Esch, & Bengtsson, 2006; Richter, Butchart, et al., 2020; Schirber, Manzini, Krismer, & Giorgetta, 2015).

Tropical gravity wave drag is therefore important in intraseasonal-to-interannual prediction models where the phase of the QBO can influence the strength of tropical convection in the Madden-Julian Oscillation (MJO) as well as Northern Hemisphere winter climate patterns (Scaife et al., 2014; Thompson & Solomon, 2002; Yoo & Son, 2016). Prediction models have also shown the QBO to be a source of skill at these timescales (Abhik & Hendon, 2019; Marshall, Hendon, & Son, 2017; Smith, Scaife, Eade, & Knight, 2016).

In summary, the QBO is a major mode of interannual variability and it is primarily driven by drag due to gravity waves emanating from tropical convection. Despite its obvious relevance to interannual climate variability, only four of the models participating in the Coupled Model Intercomparison Project-5 (CMIP5) included an internally generated QBO (Kawatani & Hamilton, 2013), and those four models obtained a QBO only through parameterization of gravity wave drag from tropical wave sources. While the number of models that are able to simulate the QBO in CMIP6 has increased to 15, the fidelity of the average QBO simulation has not improved (Richter, Anstey, Butchart, Kawatani, et al., 2020). Some climate models now parameterize drag forces due to waves emanating from convective clouds in a sophisticated way by coding the theoretical relationships between latent heating and gravity wave momentum fluxes into their gravity wave parameterizations (Beres, Garcia, Boville, & Sassi, 2005; Bushell et al., 2015; Chun, Choi, & Song, 2008; Richter, Solomon, & Bacmeister, 2014). However, it remains a very chal-

lenging problem to predict the global circulation effects of subgrid-scale or under-resolved waves that are forced by subgrid-scale latent heating, which is itself a parameterized process in global models.

Observational constraints for the important properties of the unresolved tropical gravity waves are lacking. The sources for these waves are related to the strength, size, and temporal variations in individual localized convective rain cells. Due to the multiple layers of uncertainty, parameters in tropical gravity wave schemes are often prescribed or tuned in order to achieve realistic representations of the historial QBO. Resulting QBO circulations can be extremely sensitive to the chosen parameters (Giorgetta & Doege, 2005), and the model vertical and horizontal resolutions (Holt et al., 2016, 2020; Kawatani et al., 2010). As a result, predicted changes to the QBO in future climate scenarios can differ dramatically among different models (Richter, Butchart, et al., 2020; Schirber et al., 2015). The parameterization tuning process can be a frustrating, time-consuming, and ultimately unsatisfactory method for obtaining an internally-generated QBO in climate models.

In this work, we seek to untangle uncertainties in the unresolved waves from uncertainties in the properties of unresolved convective rain cells and convective latent heating. In particular, we examine wave properties predicted by the "Beres scheme" (Beres, Alexander, & Holton, 2004; Beres et al., 2005), which is used in parameterization of convection-related gravity waves in the Whole Atmosphere Community Climate Model version 6 (WACCM6) developed at the National Center for Atmospheric Research (Gettelman et al., 2019). We examine gravity waves predicted by the Beres scheme both inside WACCM6 as well as those from "offline" calculations with the scheme, outside of the model. Our offline calculations couple the Beres scheme to the properties of convective latent heating retrieved from satellite observations. We compare model estimates of the gravity wave momentum flux and its spectrum to gravity wave properties derived from long-duration super-pressure balloon measurements in the lower stratosphere, and the comparison points to important differences between subgrid-scale convective latent heating in WACCM6 and latent heating derived from satellite observations.

The paper is organized as follows: Section 2 summarizes the approach we use in this study. Section 3 describes the models and data employed, and section 4 presents the comparisons between modelled and observed gravity waves and latent heating estimates. Section 5 explores the effects of some of the necessary assumptions behind the different latent heating estimates, and shows a way to bring the observed and modeled estimates into closer to agreement. Finally, a summary and conclusions with implications for future work are presented in Section 6.

2 Methods

Several advanced tropical gravity wave schemes have been developed that couple the properties of unresolved waves to the convective rain/latent heating parameterization in the global model. We focus on one of these in particular, the "Beres scheme" (Beres et al., 2005) developed for WACCM6, and implemented in WACCM since version 2 (Beres et al., 2005). In the most recent version, WACCM6 (Gettelman et al., 2019), the Beres scheme for gravity waves generated by convection remains coupled to the model's deep convection scheme (Zhang & McFarlane, 1995).

Figure 1 summarizes the approach used in this study. The Beres scheme is based on the linear theoretical response of the stable atmosphere to a localized, time-dependent heat source in a mean flow (Beres et al., 2004). Currently in WACCM6, fixed values for the horizontal size of rain cells (σ_x) and a red frequency spectrum shape for the time dependence of latent heating are assumed. A reference or "Look-up" table was created (Beres et al., 2005) that gives the shape of the phase speed spectrum of gravity wave momen-

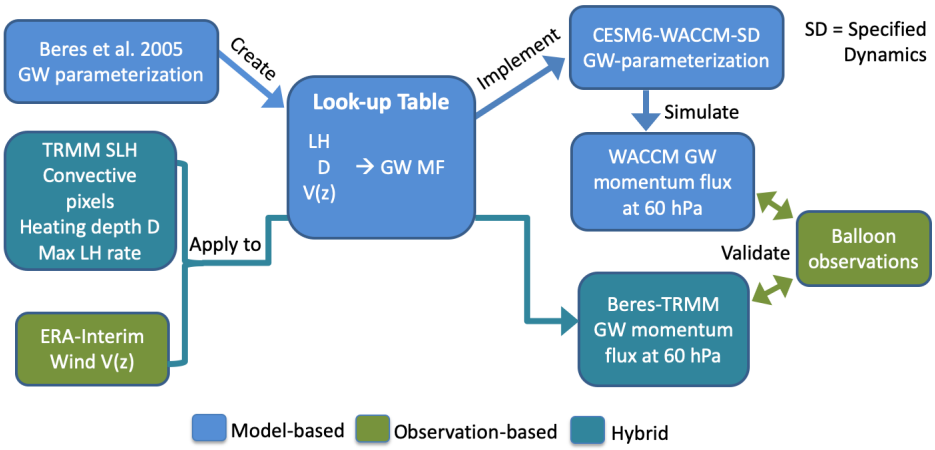

Figure 1. Flow diagram for the three estimates of gravity wave momentum flux in this paper: Parameterized waves in WACCM6 (blue), observed waves from PreConcordiasi balloons (green), and offline estimates derived by coupling TRMM latent heating with the parameterization scheme (blue-green).

tum flux for input values of the depth of the heating (D) and the mean horizontal wind (V_Q) in the layer in which the heating occurs. In WACCM6, D is based on the profile of latent heat released in a grid cell with active deep convection as parameterized with the Zhang-McFarlane scheme (Zhang & McFarlane, 1995), and V_Q is the wind in the grid cell averaged over the depth D. From the profile of grid cell latent heating rate (LH) the maximum is determined (Q), and the final output momentum flux is proportional to Q^2. In section 3 we will further detail the Beres scheme, additional assumptions, and scale factors necessary to relate grid-scale heating to subgrid-scale rain cells and gravity waves, and will also describe the WACCM6 simulation. We note here that for this work the WACCM6 model is run in a mode called "specified dynamics" (SD), where the model's winds, temperatures, and humidity are relaxed to reanalysis fields. This series of calculations (shown in blue in Fig. 1) permits direct comparison of the WACCM6 model's parameterized gravity wave properties to observations made during the PreConcordiasi campaign that took place in 2010.

In a separate series of calculations, we use the same Look-up Table and apply the same procedures in offline calculations with the Beres scheme, but base these calculations on the properties of latent heating derived from the Tropical Rainfall Measuring Mission (TRMM) Spectral Latent Heating (SLH) product (Shige, Takayabu, Tao, & Shie, 2007). This hybrid calculation, using the Beres scheme applied to observation-based latent heating, is the lower path shown in Fig. 1 with blue-green and green colors, and we call this the "Beres-TRMM" result. The mean wind in the heating layer and above is derived from global reanalysis products.

Results from these two calculations detail the local momentum fluxes for individual gravity waves, their phase speeds, the altitude at which they are launched, and the latitude, longitude, and time of their generation. From these data we derive statistics that can be directly compared to observations from long-duration super-pressure balloon flights in 2010.

3 Models and Data

3.1 Super-pressure balloon observations

In February 2010, three super-pressure balloons were launched from the Seychelle Islands for the PreConcordiasi field campaign (Jewtoukoff, Plougonven, & Hertzog, 2013). The closed balloons were filled with sufficient helium to rise to a fixed density level in the stratosphere $\sim$0.1 kg m^{-3} (approximately 60 hPa or 19.5 km). They then drifted at that level for up to several months. We use measurements from the two balloons that remained in the tropics within 15° of the equator, spanning the period from February 8 to May 11, 2010. The balloons were instrumented with geopositioning receivers with 1.5 m precision that permit retrievals of the three-dimensional wind field (u, v, w) at 30 s resolution. Because the measurements are made in the Lagrangian frame of reference, retrievals of wind perturbations as a function of intrinsic frequency $\hat{\omega}$ are possible over the entire theoretical range for gravity wave frequencies $f \leq \hat{\omega} \leq N$ where f is the Coriolis frequency and N is the buoyancy frequency. Gravity wave momentum fluxes are estimated following Vincent and Hertzog (2014) as $\bar{\rho}(\overline{u'w'}, \overline{v'w'})$. Vincent and Hertzog (2014) reported that momentum flux can be retrieved with good accuracy for intrinsic wave periods greater than $\sim$10 min, and estimated the noise floor for the momentum flux at 10^{-4} mPa. In this study, only momentum fluxes three times larger than this noise, or 3×10^{-4} mPa, are examined.

The momentum fluxes reported here differ from those previously reported in Jewtoukoff et al. (2013) in several ways: (1) Periods during the flights when the balloons temporarily lost super-pressurization, were necessarily excluded here, since the analysis assumptions do not apply in these conditions. These depressurization events occurred several times when the balloons drifted over extensive areas of high, cold cloud. Since deep cold clouds are known sources of strong gravity waves (Alexander, Beres, & Pfister, 2000), this may unfortunately eliminate some large amplitude waves. (2) We include only anomalies with frequencies between 2π/day to N. Jewtoukoff et al. (2013) also included longer period waves between f and 2π/day, where f is the Coriolis frequency. (3) The momentum flux retrieval analysis has evolved since Jewtoukoff et al. (2013) to match the method of Vincent and Hertzog (2014), which improves the accuracy of very high frequency gravity wave momentum fluxes.

3.2 Reanalysis data

Observed horizontal winds, temperature, surface pressure, and surface fluxes that are used in this study are taken from the European Center for Medium-range Weather Forecasting Reanalysis "interim" product (ERA-interim) for the period spanning Pre-Concordiasi observations (February–May 2010). ERA-interim is described in Dee et al. (2011). ERA-interim pressure level data is used for the offline calculations with the Beres parameterization scheme. For WACCM6 "specified dynamics" runs described in the next section, the 60-level native grid ERA-interim model-level data is used.

3.3 WACCM6 simulation

For this work, WACCM6 (Gettelman et al., 2019) is run in specified dynamics (SD) mode (Kunz, Pan, Konopka, Kinnison, & Tilmes, 2011; Lamarque et al., 2012), where the model's temperatures, horizontal winds, humidity and surface fluxes are relaxed over a specified pressure/altitude range at every model time-step toward reanalyzed fields. The native grid of 6-hourly ERA-interim reanalyzed fields are spatially interpolated to the WACCM6 grid and linearly interpolated to the 30-min model timestep at intermediate times. SD is a type of "nudging" where the modeled fields are relaxed to the analyzed fields with a nudging timescale of 6 hrs. The vertical range for the nudging is from Earths surface to $\sim$50 km, with the strength of the nudging reduced linearly to zero over

the 10 km above (∼50-60 km). Use of SD in WACCM6 insures that the modelled winds and stability at our altitudes of interest, below the middle stratosphere, remain close to observed, and this permits direct comparison of parameterized gravity wave properties in the simulation to observations in the lower stratosphere during the PreConcordiasi campaign in 2010. More specifically, the use of SD is important to ensure similar source regions for the gravity waves in WACCM6 and the observations, similar wind filtering of the gravity waves, and similar interactions between the wave sources and the winds (Alexander, Ortland, Grimsdell, & Kim, 2017).

Similarly to previous versions of WACCM, WACCM6 includes non-orographic gravity wave drag associated with convection according to the Beres parameterization scheme (Beres et al., 2005; Richter, Sassi, & Garcia, 2010). The Beres scheme is described in the next section.

3.4 "Beres" parameterization scheme for gravity waves from convection

The Beres scheme predicts the properties of unresolved gravity waves emanating from deep convection that occurs in a given WACCM6 grid-cell at each location and each physics time step. The basic output of the Beres scheme is the phase speed spectrum of gravity wave momentum flux at the top of the convective latent heating and the directions of wave propagation. Gravity wave properties depend on grid-scale model fields illustrated with a schematic shown in Figure 2.

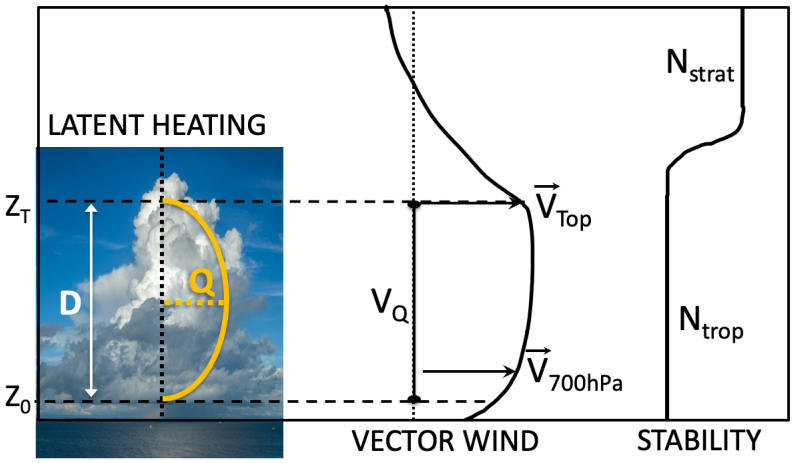

Figure 2. Schematic illustrating parameters used in the application of the Beres parameterization scheme.

The wave momentum flux is computed as a function of wave frequency (ν) and horizontal wavenumber (k) using Beres et al. (2004) (their equation 30):

$$M_{k\nu} = \frac{1}{\sqrt{2\pi}} \frac{\rho_0}{L\tau} sgn(\hat{\nu}) \left(\frac{N^2}{\hat{\nu}^2} - 1 \right)^{1/2} |B_{k\nu}|^2 \tag{1}$$

where $\hat{\nu} = \nu - kV_Q$, with V_Q the wind in the heating layer, $N = N_{trop}$ the tropospheric buoyancy frequency (=0.01 s^{-1}), ρ_0 the atmospheric density, and L and τ are spatial

and temporal averaging domains, respectively, and

$$B_{k\nu} = Q_0 Q_t(\nu) \frac{k^2}{\hat{\nu}^2} \frac{\sigma_x}{\sqrt{2}} \exp\left(\frac{-k^2\sigma_x^2}{4}\right)\left(\frac{\pi}{m_{k\nu}D}\right)\frac{\sin(m_{k\nu}D)}{(m_{k\nu}^2 - \pi^2/D^2)}. \quad (2)$$

The source momentum flux $M_{k\nu}$ is only non-zero where the convective parameterization is active and convective latent heating is non-zero. There, the heating factor $Q_0 = Q/CF$ is computed, where CF is the fraction of the grid area covered by convective rain cells and Q is the maximum in the grid-scale heating profile.

For application in WACCM6 (Beres et al., 2005), only the non-stationary gravity waves are treated, that is those that are propagating relative to the motion of the latent heating cells. The waves are assumed to be launched in two directions forward and backward of the 700 hPa wind vector ($\vec{V}_{700hPa}$). Therefore, the relevant wind in the heating layer, V_Q, is the component along that direction. The unresolved convective heating horizontal scale σ_x was set to a fixed value of 3 km, and CF set to 5%. The L and τ factors are related to the model grid scale and time step, but in practice are combined together with the ρ_0 factor into a tunable parameter $C_{L\tau}$. The spectral dependence on (k, ν) was converted to a dependence on the single variable phase speed $c = \hat{\nu}/k$ using also the dispersion relation,

$$m_{k\nu}^2 = \frac{N^2}{c^2} - k^2. \quad (3)$$

For computational efficiency, (1) is converted to a look-up table stored as a function of the model grid-scale variables V_Q and D (convective heating depth, $D = z_T - z_0$). At each grid point and time when the convective parameterization is active, a spectral array $K_{V_Q D}(c)$ is read in from the table associated with the specific local values of V_Q and D, and the launch level momentum flux computed as

$$M_0(c) = C_{L\tau} Q_0^2 K_{V_Q D}(c), \quad (4)$$

with the launch level assumed to be at the top of the convective heating (z_T) (Richter et al., 2010). The flux spectrum $M_0(c)$ is treated with a discrete set of 64 phase speeds c_j ranging from ± 80 m s^{-1} at 2.5 m s^{-1} intervals. Each discrete wave is assumed to propagate vertically within the column. Momentum flux for each phase speed $M_j(z)$ is conserved unless the flux exceeds a limit set by the Lindzen (1981) saturation criterion (Holton, 1982). The drag force profile $F(z)$ on the mean flow is computed from the vertical gradient of the total flux as,

$$F(z) = \frac{-\epsilon}{\rho_0(z)} \frac{d}{dz}\left(\Sigma_j M_j(z)\right), \quad (5)$$

with ϵ an efficiency factor that tunes the force, currently set to 0.5 in WACCM6. Gettelman et al. (2019) also note that to improve the simulation of the QBO, the factor D is multiplied by 0.25 in the reference to the look-up table, which has the effect of emphasizing lower phase speed waves in the spectrum.

3.5 Satellite-based precipitation and latent heating

Latent heating derived from satellite-based radar precipitation measurements are available through the Tropical Rainfall Measuring Mission (TRMM) for our period of interest in 2010. The Spectral Latent Heating (SLH) product (Shige, Takayabu, Tao, & Johnson, 2004) gives estimates of instantaneous convective latent heating profiles at TRMM radar footprint locations. TRMM radar footprints are 4.3 km diameter, a very similar scale as the 3-km diameter convective updraft scale (σ_x) assumed in the Beres scheme. The SLH algorithm identifies convective rain by the absence of a bright band in the PR reflectivity, and isolated rain cells in the tropics are also labelled as convective (Awaka, Kumagai, & Iguchi, 2009). The profile of latent heating is derived from the PR echo-top height and surface rain rate together with a look-up table that was based on cloud-reolving simulations.

While the SLH approach could have large uncertainties in the individual instantaneous LH profiles due to timing mismatches between the water phase change process and the presence of the large hydrometeors detectable by radar, these retrievals successfully utilize constraints from radar observables and may provide reasonable LH vertical structures in a statistical sense (Liu, Shige, Takayabu, & Zipser, 2015; Shige et al., 2009; Takayabu, Shige, Tao, & Hirota, 2010). Details of the SLH retrieval algorithm are described in Shige et al. (2004, 2009, 2007); Shige, Takayabu, Tao, and Shie (2008).

For our study, the results will be most sensitive to the strongest localized convective rain cells, since these are the most efficient gravity wave generators. Stratiform rain tends to be weaker, cover larger horizontal areas, and evolve on slower time scales, so stratiform heating is not likely to be an important source of small-scale gravity waves, and we neglect stratiform heating here. One of the main uncertainties in using SLH for this study may be the limited number and type of cloud-resolving simulations that were the basis for the look-up table. However, the SLH product is a well-studied global observation-based latent heating product useful for defining small-scale instantaneous convective latent heating rates. It provides independent information on convective gravity wave sources, and gives us a way to separately validate the gravity wave scheme without its dependence on the WACCM convection parameterization and the additional assumptions about the subgrid-scale properties of the convection.

4 Results

4.1 Distribution of Momentum Fluxes

Observations of gravity wave momentum fluxes have previously revealed that large amplitude gravity waves in the lower stratosphere are highly intermittent, and a large fraction of the total momentum flux is carried by only a small fraction of the wave events (Hertzog, Alexander, & Plougonven, 2012). These large amplitude waves will tend to break at lower altitudes, and may be one of the keys to realistic global simulations of the stratospheric circulation (de la Cámara, Lott, Jewtoukoff, Plougonven, & Hertzog, 2016), and key to improving shortcomings in simulations of the QBO (Bushell et al., 2020).

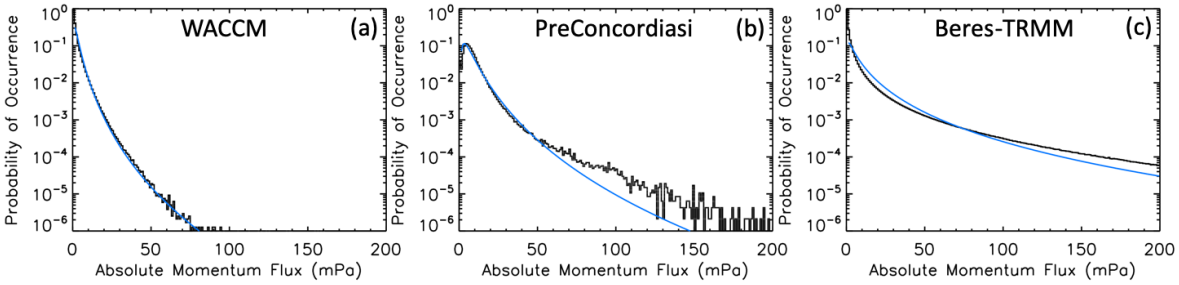

Figure 3. Occurrence frequencies of gravity wave momentum flux at a level near 60 hPa. (a) Parameterized waves in WACCM6-SD. (b) Observed waves from PreConcordiasi balloons. (c) Offline estimates derived by coupling TRMM convective latent heating with the parameterization scheme. Blue lines show the log-normal distributions with the same means and standard deviations computed using only values larger than 1 mPa.

Figure 3 compares distributions of occurrence frequency of absolute gravity wave momentum flux for individual gravity waves at pressure levels near 60 hPa. As seen in previous studies, the PreConcordiasi observations (Fig. 3b) display a long tail of very large but infrequent momentum fluxes. In the data, each flux represents a value at a unique

Table 1. Tropical (15S-15N) unconditional mean gravity wave momentum fluxes for the three estimates: eastward waves (E), westward waves (W), total absolute zonal (|E|+|W|), asymmetry factor 2*(E+W)/(E−W), and total omni-directional (|E|+|W|+|N|+|S|). The table also includes and the standard deviation (SD) about the mean of all non-zero values.

Estimate Type	E (mPa)	W (mPa)	|E|+|W| (mPa)	Asymmetry Factor	|E|+|W|+|N|+|S| (mPa)	SD (mPa)
WACCM6-SD*	0.8	−1.1	1.9	−0.4	3.0	1.5
PreConcordiasi	2.6	−3.0	5.6	−0.2	8.9	8.4
Beres-TRMM	1.3	−1.2	2.5	+0.1	3.8	8.5

* Fluxes do not include the WACCM6 efficiency factor=0.5.

time, and fluxes are computed at 1 min intervals. In the atmosphere, the spectrum of waves emanating from a single convective source will disperse according to their properties, following different group velocity vector paths. So waves with different frequencies and phase speeds appear at different locations and times away from that source. The parameterized waves are assumed to remain in one grid-scale column of air and travel instantly through the depth of the column in order to estimate the force on the flow. Fluxes computed from the parameterization in Figs. 3a and c represent instantaneous values at each phase speed in the spectrum. Since each of these is treated as an independent monochromatic wave, this provides the closest comparison to the observed wave fluxes. In contrast to the data, the Beres scheme's gravity waves in WACCM6-SD (Fig. 3a) at the nearest pressure level (61 hPa) are missing the largest momentum flux values greater than 100 mPa.

Fig. 3c shows the gravity wave momentum fluxes resulting from the Beres-TRMM method, which are computed with the Beres-scheme run offline and using TRMM SLH heating and ERA-interim winds and stability (N) to define the sources, propagation to 60 hPa, and dissipation due to saturation according to the Beres scheme (Beres et al., 2005). This result shows a very long tail of large momentum fluxes that are missing in the Beres scheme in WACCM6-SD (Fig. 3a). Since the ERA-interim winds and stability are approximately the same in both Figs. 3a and c, the difference seems to point to deficiencies in the heating rates Q_0 in the WACCM6-SD run.

Blue lines in Fig. 3 show the lognormal distributions with the same means and standard deviations as the black histograms. Note that these statistics are computed only using fluxes greater than 0.5 mPa because unlike the observations, the parameterized occurrence frequencies increase continually to the very lowest values. Why this peak at very low values is not seen in the data is not completely understood, but may be related to wave dispersion that spreads signals, which ensures there is always some larger signal present at the same time as the very weak signals, and the larger signal is preferentially detected. In the data there are very few occurrences of flux close to the reported noise floor at 1×10^{-4} mPa (Vincent & Hertzog, 2014).

Table 1 compares statistical details of the momentum fluxes among the three results: Observations, Beres-WACCM6-SD, and Beres-TRMM. The zonal (E and W) components of the flux are particularly relevant to the forcing of the QBO. The Beres-TRMM method has larger fluxes than the WACCM6-SD gravity waves, but both are smaller than observed. The standard deviation in the Beres-TRMM fluxes is very similar to the observations, and this follows from the more similar long tail of large flux values that was noted in Fig. 3. The east versus west asymmetry factor is small in the observations and is negative (more westward flux than eastward flux). WACCM6-SD is larger but also neg-

ative, while Beres-TRMM has a slight positive asymmetry factor. We will revisit this asymmetry in the Discussion section 5.

4.2 Momentum Flux Phase Speed Spectra

Figure 4 compares the zonal mean phase speed spectrum of zonal momentum flux in the three results. These spectra are normalized such that the absolute flux sums to equal the |E|+|W| column in Table 1. The Beres-TRMM result (blue) looks similar to the observations (green) at the higher phase speeds, but there appears to be missing flux at low phase speeds. The WACCM6-SD result (red) has more flux at low phase speeds, but is missing flux from higher phase speed waves. Recall that in WACCM6 (Gettelman et al., 2019), the heating depth D was artificially reduced by a factor of 4 in order to obtain a realistic QBO period and amplitude. In the Beres scheme, $D \propto m^{-1}$ and considering the gravity wave dispersion relation, $m^{-1} \propto c$, so choosing 0.25D will focus the momentum fluxes into the slower phase speed portion of the wave spectrum, and this was apparently necessary to simulate a QBO in WACCM6 (Gettelman et al., 2019; Mills et al., 2017).

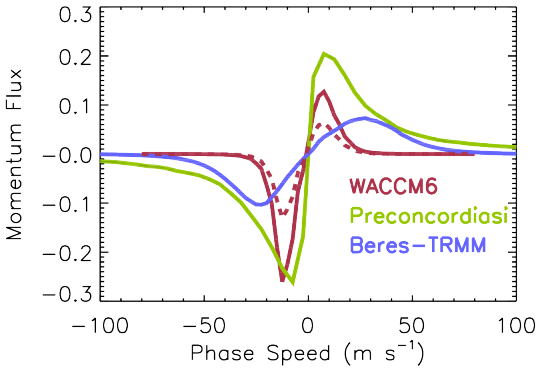

Figure 4. Phase speed spectra of zonal momentum flux for WACCM6 (red), PreConcordiasi (green), and Beres-TRMM (blue). For WACCM6 and Beres-TRMM, only grid points with convective precipitation contribute to the spectrum, so each spectrum is normalized by the unconditional absolute zonal mean zonal flux (|E|+|W| in Table 1). Red dashed line shows WACCM6 after multiplication by the efficiency factor=0.5.

For reference, Fig. 4 also shows the WACCM6-SD momentum flux after multiplication by the efficiency factor ϵ as the red dashed line. Note that the flux amplitudes plotted in Fig. 3 are used in WACCM6 to determine the altitude where gravity waves break, but the force (5) is scaled by this efficiency factor. We therefore show the spectrum scaled by the efficiency factor in Fig. 4 because these are zonal mean fluxes that are relevant to the net momentum forcing budget. We also note that while free-running WACCM6 does include a QBO because of these parameterized gravity wave forces, the amplitude is too weak and it does not extend to low enough altitudes (see Gettelman et al. (2019) their Fig. 6). We will return to the relevance of the gravity wave phase speed spectrum to simulating the QBO in section 5.

4.3 Distributions of Convective Latent Heating

The comparison of momentum fluxes in Fig. 3 suggested that values of Q_0 in the WACCM6 Beres scheme are missing the large but infrequent heating rates that give the

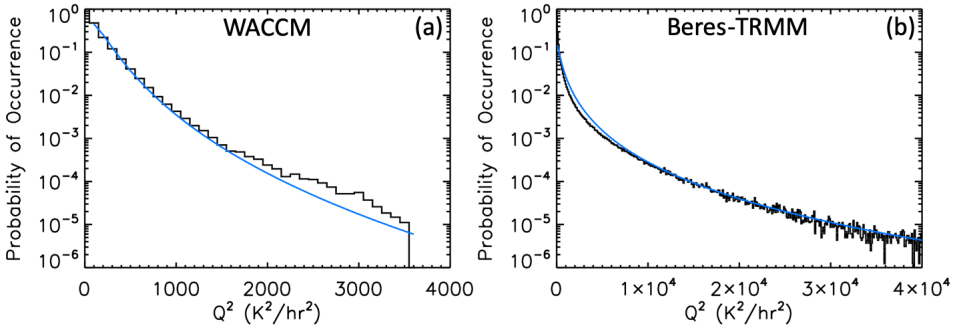

Figure 5. Occurrence frequencies of latent heating squared (Q_0^2) where Q_0 is the maximum rate (K/hr) in the heating profile associated with the parameterized grid-scale convection divided by the convective fraction, CF. According to the assumptions in the WACCM6 application of the Beres parameterization, the subgrid-scale plumes have 3 km diameter and occupy 5% of the $1^\circ \times 1^\circ$ grid box so CF=.05, and wave momentum flux is proportional to Q_0^2. The blue curves are log-normal fits to the distributions excluding the smallest bin.

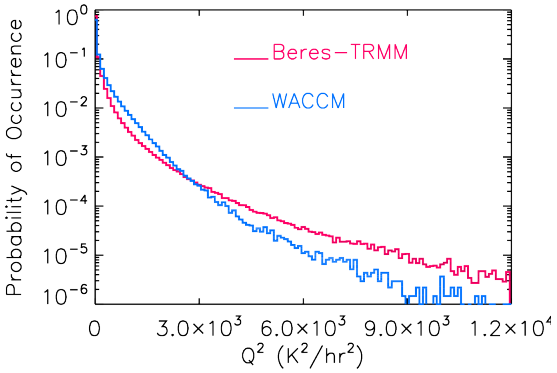

Figure 6. Distributions of latent heating squared (Q_0^2) in convective cells, exploring uncertainties in assumed parameters. The red curve shows TRMM heating without the area correction factor that accounted for the difference between TRMM footprint size and parameterization plume scale σ_x (i.e. no correction for under-resolved convective plumes). The blue curve shows WACCM6-SD heating assuming that the convective area fraction of $1^\circ \times 1^\circ$ grid cells is reduced from 5% to 3%.

large but infrequent values of momentum flux. Figure 5 compares the frequency of the square of these latent heating rates in WACCM6-SD and in the TRMM SLH convective pixels that were used in the Beres-TRMM calculations. We show the square of the heating because it is proportional to the momentum flux (4). Both panels represent the local convective plume-scale heating rates in (4). For Fig. 5a, we plot the grid-scale maximum heating divided by the convective fraction, $Q_0 = Q/CF$. For Fig. 5b, this is the area of the 4.5 km scale TRMM SLH heating normalized by the assumed convective scale σ_x=3 km, or $[(4.5/3)^2 Q]^2$. Both distributions follow the lognormal shape (blue curves), which explains the same shape of the distributions seen in the momentum fluxes (Fig. 3). SLH-based values input to the Beres-TRMM calculations are more than 10 times larger, and this likely explains the differences seen in the momentum fluxes between these two results.

To examine the effect of some of the necessary assumptions about convective plume scales, we show WACCM6-SD with a convective fraction reduced to 3% in Figure 6 and compare this to Beres-TRMM heating rates without the area normalization factor. The two distributions are now quite similar, indicating a high sensitivity to these assumptions, and a similar high sensitivity in the momentum flux distributions through (4).

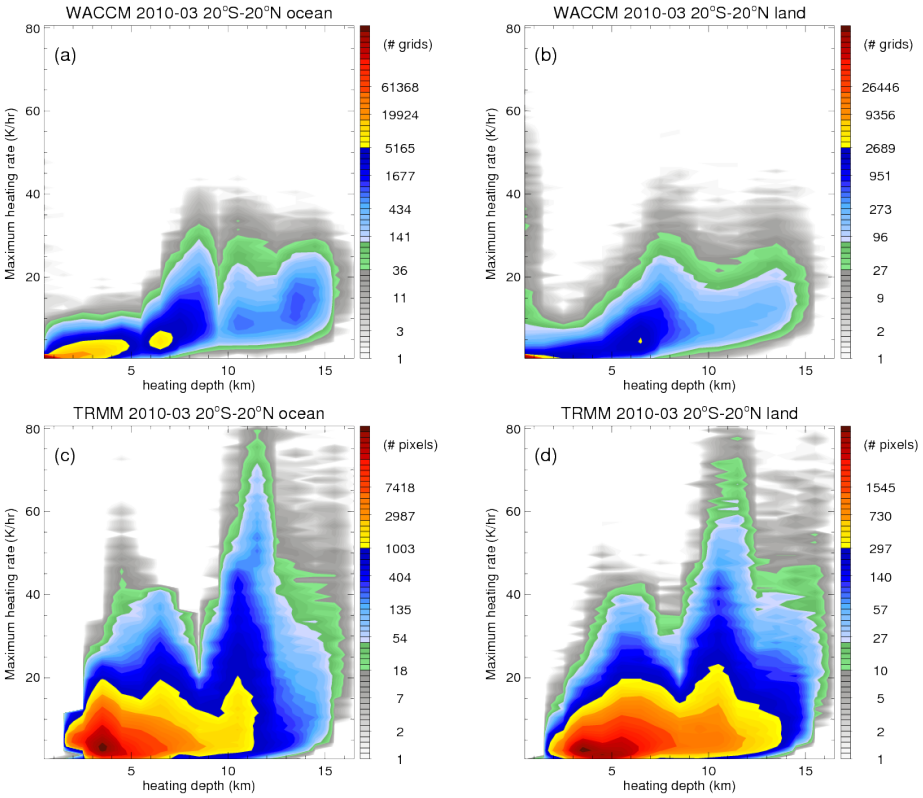

Figure 7. Occurrence frequencies of convective heating as a function of heating depth and maximum heating rate for WACCM6 (top row) and TRMM SLH (bottom row). Distributions over ocean (left column) and land (right column) are shown separately.

Figure 7 shows frequency distributions of convective heating as a function of heating depth and maximum heating rate comparing WACCM6-SD Q_0 properties to TRMM SLH convective pixels for the same 2010 PreConcordiasi period. For WACCM6, the artificial factor of 0.25 on depth that was used to compute gravity wave momentum fluxes is not applied in this figure. Distributions of depths are similar in the model and observed, with overall depths mostly below 16 km and a peak in the shallow cumulus range below 5km. At the strongest convective heating rates (representing the strongest gravity wave sources), WACCM6-SD depths show three peaks over ocean and two peaks over land between 8-15 km. TRMM show similar peaks over ocean and land near 6 km and 11.5 km, and a lesser peak only over land near 15 km. Overall, with the exception of the weaker heating magnitudes in WACCM6-SD, the distributions are fairly similar. This comparison would support the choice of a smaller assumed convective fraction, closer to 3%, that was explored in Fig. 6, which would effectively increase the WACCM6 convective heating rates in Fig. 7 by a factor of 5/3.

5 Discussion

The comparison of convectively generated gravity wave spectra of zonal momentum fluxes in Fig. 4 has interesting implications for the Beres parameterization method and for the simulation of the QBO in WACCM6 that we explore further in this section. The comparison of the green and blue spectra suggests that the Beres scheme (as it is currently formulated in WACCM6) can produce a realistic spectrum of fast waves, those with phase speeds greater than $\sim$20 m s^{-1}, when the unresolved convective latent heating sources are defined in a realistic way (i.e. based on TRMM observations), but that slower phase speed waves are grossly under-represented. The red spectrum, which is the spectrum of Beres scheme waves in WACCM6 that results when the WACCM6 heating depths were divided by 4, suggests that WACCM6 needs forcing from these otherwise missing low phase speed waves in order to simulate a QBO-like oscillation (Gettelman et al., 2019; Mills et al., 2017).

The Beres scheme as represented in WACCM6 (Beres et al., 2005) omitted the contribution of stationary gravity waves, those that are stationary relative to the motion of the convective rain cells. While Beres et al. (2004) included a formulation for these stationary waves, they were omitted in the Beres et al. (2005) WACCM (versions 2 through 6) application because of large uncertainties involved in estimating the fluxes from these waves. The stationary wave momentum fluxes are highly sensitive to the details of the wind profile near the top of the convection. Further, when upper level shear is present, which results in the largest fluxes, the result is also highly sensitive to the exact depth of penetration of the unresolved, subgrid-scale convective latent heating into the shear layer. In addition, it is common wisdom that the non-stationary spectrum of gravity waves is necessary to obtain realistic amplitudes of the QBO and the semi-annual oscillations that occur above the QBO in the tropical middle atmosphere. Studies applying only the stationary component of convectively generated gravity waves showed significant forces in the upper troposphere and lower stratosphere but failed to generate a QBO-like oscillation (Chun, Song, Baik, & Kim, 2004).

Convection- and gravity-wave-resolving model studies have however suggested this stationary wave component may be an important or even dominant contributor to the gravity wave momentum flux above deep convection (Alexander, Richter, & Sutherland, 2006; Kuester, Alexander, & Ray, 2008). The stationary wave momentum flux will also tend to concentrate at the slower phase speeds that appear to be missing from the non-stationary wave component (Fig. 4). In particular, Alexander et al. (2006) found that for a simulation over tropical Australia, the stationary wave fluxes appeared as a strong peak in flux concentrated near 5-10 m s^{-1} phase speeds, which stood out well above the background non-stationary wave spectrum, however that study was not able to put any quantitative values on the strength of that peak due to uncertainties in the convective latent heating.

To explore the possible effects of the missing stationary component of gravity wave momentum fluxes, we compute the flux following Beres et al. (2004) using TRMM SLH to define the heat source properties and ERA-interim winds to define the wind profile. The use of observations to define the winds and properties of convective latent heating removes much of the uncertainty in the estimate of the flux described above, however the fluxes from this mechanism are known to respond nonlinearly to the strength of the heating (Alexander et al., 2006), while the Beres et al. (2004) formula is based on linear theory. We therefore compute the stationary wave spectrum based on detailed observed properties, which we expect will give robust features to the shape of the resulting wave spectrum, but the amplitudes remain uncertain.

Figure 8 shows the resulting zonal-mean phase speed spectrum of zonal momentum flux as a function of ground-based phase speed averaged over the Preconcordiasi period in 2010. The spectrum is normalized to sum to unity, because we can only discuss

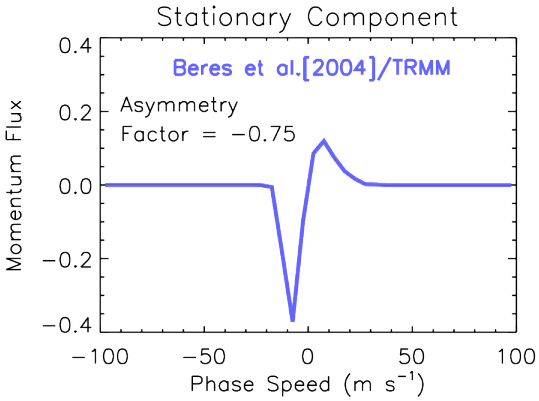

Figure 8. Normalized zonal mean phase speed spectrum of stationary wave ($\nu = 0$) zonal momentum flux relative to the convective heating cells using TRMM SLH to define the convective latent heating sources and ERA-Interim to define the winds. The equations for momentum flux for these stationary waves are given in Beres et al. (2004), and the spectrum is computed at the 60 hPa level.

the spectrum shape and east-to-west asymmetries rather than any net flux effects on the QBO. The stationary wave spectrum peaks at low phase speeds less than 10 m s^{-1}, with little flux occurring at phase speeds higher than 20 m s^{-1}. The spectrum also shows significant east-to-west asymmetry, with a preference towards westward wave flux (asymmetry factor = -0.75). In summary, if this stationary component has significant amplitude, then adding it to the non-stationary component (Beres-TRMM in Fig. 4) could reproduce many of the properties seen in the Preconcordiasi observations.

Adding the stationary wave component could also eliminate the need for the artificial reduction in heating depth that was applied in WACCM6 in order to generate a QBO-like oscillation. The QBO in WACCM6 has very weak amplitudes, which could be improved by retaining the more realistic high phase speed fluxes. Also, the WACCM6 QBO almost disappears as it descends below ∼50 hPa (Gettelman et al., 2019), a very common problem in simulations of the QBO (Bushell et al., 2020). It is the strength of the QBO at these lowermost stratosphere levels near the tropopause that is believed to be responsible for influencing the MJO, and the poor representation of the QBO at these levels may be responsible for the under-representation of QBO influences in models on subseasonal-to-seasonal climate (Abhik & Hendon, 2019; Richter et al., 2014; Smith et al., 2016). We also note that while higher vertical resolution in specialized WACCM experiments (Richter et al., 2014) improved the strength of eastward QBO winds in the lower stratosphere, the westward wind phase tends to be weak and short duration, suggesting that enhanced westward parameterized gravity wave momentum flux associated with adding the stationary component (Fig. 8) might lead to further improvements in the simulation of the QBO in the lower stratosphere, and might be used as a tool to improve the QBO in WACCM6 experiments where high vertical resolution is impractical.

6 Summary and Conclusions

In some climate models like WACCM6, parameterized tropical gravity waves are directly related to the properties of parameterized convective latent heating using the Beres scheme. Through detailed comparisons of the parameterized gravity waves to superpressure balloon observations we find clear discrepancies in the total momentum fluxes (Table 1), the occurrence frequencies of large-amplitude gravity waves (Fig. 3), and the

zonal-mean phase speed spectrum of zonal momentum flux (Fig. 4), all of which are key factors in the ability of the parameterized waves to drive a realistic QBO circulation.

Through additional comparisons of WACCM6-SD parameterized tropical convective latent heating to satellite data products, we find many similarities (Fig. 7), but the assumption of how that heating is distributed at the subgrid-scale that influences the parameterized gravity wave amplitudes (Fig. 5) could be adjusted (Fig. 6) to correct deficiencies in occurrence frequencies of the larger-amplitude waves. We further hypothesize these large amplitude waves may be important both in achieving more realistic QBO wind amplitudes in models, particularly at the lower reaches of the QBO $\sim 50 - 100$ hPa. Most models, including WACCM6, display QBO amplitudes that are much too weak at these levels.

The phase speed spectrum of Beres scheme parameterized tropical gravity waves in WACCM6-SD is quite different from the phase speed spectrum computed using offline calculations of the Beres scheme driven by satellite-based latent heating properties (Fig. 4). In particular the WACCM6-SD waves cluster at low phase speeds (c) while waves from the offline calculation cluster at higher c. The reason is primarily because of the artificial reduction by a factor of 4 applied to the latent heating depth parameter (D) within the Beres scheme in WACCM6, which serves to shift wave momentum fluxes to much slower c. Note that in the Beres scheme $D \propto m^{-1}$ and $m^{-1} \propto c$ through (3). This shift to lower phase speeds permitted simulation of a more realistic QBO in the free-running WACCM6 (Gettelman et al., 2019).

In section 5, we suggest an alternate way to increase gravity wave momentum fluxes at low c. The current Beres scheme omits the component of convectively generated gravity waves that are stationary relative to convective rain cells. Offline calculations of this component of the convective gravity wave spectrum (Fig. 8) show these waves would peak at the desired low $|c| \leq 10$ m s^{-1}. Adding this component to the existing non-stationary Beres scheme waves could provide excellent agreement with the super-pressure balloon observations, and has the potential to also improve simulations of both the strength of the QBO and depth of penetration of the QBO to lower altitudes near the tropopause, which are common current weaknesses in most state-of-the-art climate models that simulate the QBO (Bushell et al., 2020). Implementation of the the WACCM6 Beres scheme changes that our results suggest is currently being explored and will be addressed in a separate publication.

Finally, we suggest that the failure of most climate and seasonal forecast models to simulate realistic QBO amplitudes in the lowermost stratosphere is a likely cause for the failure in models to represent realistic QBO impacts on surface weather and climate (Alexander & Holt, 2019). These include QBO influences on the strength and duration of MJO rain events and other influences of the QBO on winter weather in the Northern Hemisphere. Thus improvements in the parameterization of tropical convectively generated gravity waves such as we propose here have the potential to improve subseasonal to interannual climate prediction, as well as improve the representation of natural variability in long-term climate simulations.

Acknowledgments

This work was funded by a grant from the National Science Foundation's programs in Large-Scale Climate Dynamics and Physical & Dynamical Meteorology under award 1829373. The CESM project is supported primarily by the National Science Foundation (NSF). This material is based upon work supported by the National Center for Atmospheric Research, which is a major facility sponsored by the NSF under Cooperative Agreement 1852977. The TRMM SLH data are processed and distributed by NASA at `https://pps.gsfc.nasa.gov/`. The collocated TRMM and ERA-Interim data are available at

http://atmos.tamucc.edu/trmm/. Superpressure balloons flights were performed within the Concordiasi project, which was supported by Météo-France, CNES, CNRS/INSU, NSF, NCAR, University of Wyoming, Purdue University, University of Colorado, the Alfred Wegener Institute, the Met Office, and ECMWF. The superpressure balloon measurements (described in Podglajen, Plougonven, Hertzog, and Legras (2016)) is available via https://data.mendeley.com/datasets/2w7ftt9jzk/1.

References

Abhik, S., & Hendon, H. H. (2019). Influence of the QBO on the MJO during coupled model multiweek forecasts. *Geophys. Res. Lett.*, *46*(15), 9213-9221. doi: 10.1029/2019GL083152

Alexander, M. J., Beres, J. H., & Pfister, L. (2000). Tropical stratospheric gravity wave activity and relationship to clouds. *J. Geophys. Res.*, *105*(D17), 22,299-22,309.

Alexander, M. J., & Holt, L. A. (2019). The quasi-biennial oscillation and its influences at the surface. *US Clivar Variations*, *17*(1), 20-26. doi: 10.5065/q3jb-9642

Alexander, M. J., Ortland, D. A., Grimsdell, A. W., & Kim, J.-E. (2017). Sensitivity of gravity wave fluxes to interannual variations in tropical convection and zonal wind. *J. Atmos. Sci.*, *74*, 2710–2716. doi: 10.1175/JAS-D-17-0044.1

Alexander, M. J., Richter, J. H., & Sutherland, B. R. (2006). Generation and trapping of gravity waves from convection, with comparison to parameterization. *J. Atmos. Sci.*, *63*(11), 2963-2977.

Awaka, J., Kumagai, H., & Iguchi, T. (2009). TRMR standard algorithm 22A3 and its performance on bright band detection. *J. Meteor. Soc. Japan*, *87A*, 31-52. doi: 10.2151/jmsj.87A.31

Beres, J., Alexander, M. J., & Holton, J. R. (2004). A method of specifying the gravity wave spectrum above convection based on latent heating properties and background wind. *J. Atmos. Sci.*, *61*, 324-337.

Beres, J., Garcia, R., Boville, B., & Sassi, F. (2005). Implementation of a gravity wave source spectrum parameterization dependent on the properties of convection in the whole atmosphere community climate model (WACCM). *J. Geophys. Res.*, *110*(D10108), doi:10.1029/2004JD005504.

Bushell, A. C., Anstey, J. A., Butchart, N., Kawatani, Y., Osprey, S. M., Richter, J. H., ... Yukimoto, S. (2020). Evaluation of the quasi-biennial oscillation in global climate models for the SPARC QBO-initiative. *Q. J. Roy. Meteorol. Soc.*, *146*(1-31), . doi: 10.1002/qj.3765

Bushell, A. C., Butchart, N., Derbyshire, S. H., Jackson, D. R., Shutts, G. J., Vosper, S. B., & Webster, S. (2015). Parameterized gravity wave momentum fluxes from sources related to convection and large-scale precipitation processes in a global atmosphere model. *J. Atmos. Sci.*, *72*(11), 4349-4371. doi: 10.1175/JAS-D-15-0022.1

Butchart, N., Anstey, J. A., Hamilton, K., Osprey, S., McLandress, C., Bushell, A. C., ... Yukimoto, S. (2018). Overview of experiment design and comparison of models participating in phase 1 of the SPARC quasi-biennial oscillation initiative (QBOi). *Geosci. Model Dev.*, *11*(3), 1009–1032. Retrieved from https://www.geosci-model-dev.net/11/1009/2018/ doi: 10.5194/gmd-11-1009-2018

Chun, H.-Y., Choi, H.-J., & Song, I.-S. (2008). Effects of nonlinearity on convectively forced internal gravity waves: Application to a gravity wave drag parameterization. *J. Atmos. Sci.*, *65*(2), 557-575. doi: 10.1175/2007JAS2255.1

Chun, H.-Y., Song, I.-S., Baik, J.-J., & Kim, Y.-J. (2004). Impact of a convectively forced gravity wave parameterization in NCAR CCM3. *J. Climate*, *17*(18), 3530-3547.

Dee, D. P., Uppala, S. M., Simmons, A. J., Berrisford, P., Poli, P., Kobayashi, S., ... others (2011). The ERA-interim reanalysis: configuration and performance of the data assimilation system. *Q. J. Roy. Meteorol. Soc.*, *137*(656), 553597.

de la Cámara, A., Lott, F., Jewtoukoff, V., Plougonven, R., & Hertzog, A. (2016). On the gravity wave forcing during the southern stratospheric final warming in LMDZ. *J. Atmos. Sci.*, *73*(8), 3213-3226. doi: 10.1175/JAS-D-15-0377.1

Gettelman, A., Mills, M. J., Kinnison, D. E., Garcia, R. R., Smith, A. K., Marsh, D. R., ... Randel, W. J. (2019). The Whole Atmosphere Community Climate Model version 6 (WACCM6). *J. Geophys. Res. Atmos.*, *124*, 12,380–12,403. doi: 10.1029/2019JD030943

Giorgetta, M. A., & Doege, M. C. (2005). Sensitivity of the quasi-biennial oscillation to CO_2 doubling. *Geophys. Res. Lett.*, *32*(L08701), doi:10.1029/2004GL021971.

Giorgetta, M. A., Manzini, E., Roeckner, E., Esch, M., & Bengtsson, L. (2006). Climatology and forcing of the quasi-biennial oscillation in the MAECHAM5 model. *J. Climate*, *19*(16), 3882-3901.

Hertzog, A., Alexander, M. J., & Plougonven, R. (2012). On the intermittency of gravity-wave momentum flux in the stratosphere. *J. Atmos. Sci*, *69*, 3433-3448.

Holt, L. A., Alexander, M. J., Coy, L., Molod, A., Putman, W., & Pawson, S. (2016). Tropical waves and the quasi-biennial oscillation in a 7-km global climate simulation. *J. Atmos. Sci.*, *73*, null. doi: 10.1175/JAS-D-15-0350.1

Holt, L. A., Lott, F., Garcia, R. R., Kiladis, G. N., Cheng, Y.-M., Anstey, J. A., ... Yukimoto, S. (2020). An evaluation of tropical waves and wave forcing of the QBO in the QBOi models. *Q. J. Roy. Meteorol. Soc.*, *146*, 1–27. doi: 10.1002/qj.3827

Holton, J. (1982). The role of gravity wave induced drag and diffusion in the momentum budget of the mesosphere. *J. Atmos. Sci.*, *39*, 791-799.

Jewtoukoff, V., Plougonven, R., & Hertzog, A. (2013). Gravity waves generated by deep tropical convection: Estimates from balloon observations and mesoscale simulations. *J. Geophys. Res. Atmos.*, *118*(17), 9690–9707. doi: 10.1002/jgrd.50781

Kawatani, Y., & Hamilton, K. (2013). Weakened stratospheric quasibiennial oscillation driven by increased tropical mean upwelling. *Nature*, *497*, 478–481.

Kawatani, Y., Sato, K., Dunkerton, T. J., Watanabe, S., Miyahara, S., & Takahashi, M. (2010). The roles of equatorial trapped waves and three-dimensionally propagating gravity waves in driving the quasi-biennial oscillation. PART I: zonal mean wave forcing. *J. Atmos. Sci.*, *67*(DOI:10.1175/2009JAS3222.1), 963-980.

Kuester, M., Alexander, M., & Ray, E. (2008). A model study of gravity waves over hurricane Humberto (2001). *J. Atmos. Sci.*, *65*, 3231-3246.

Kunz, A., Pan, L. L., Konopka, P., Kinnison, D. E., & Tilmes, S. (2011). Chemical and dynamical discontinuity at the extratropical tropopause based on START08 and WACCM analyses. *J. Geophys. Res.*, *116*, D24302. doi: 10.1029/2011JD016686

Lamarque, J.-F., Emmons, L. K., Hess, P. G., Kinnison, D. E., Tilmes, S., Vitt, F., ... Tyndall, G. K. (2012). CAM-chem: description and evaluation of interactive atmospheric chemistry in the Community Earth System Model. *Geosci. Model Dev.*, *5*, 369–411.

Lindzen, R. S. (1981). Turbulence and stress owing to gravity wave and tidal breakdown. *J. Geophys. Res.*, *86*, 9707-9714.

Liu, C., Shige, S., Takayabu, Y. N., & Zipser, E. (2015). Latent heating contribution from precipitation systems with different sizes, depths, and intensities in the tropics. *J. Climate*, *28*(1), 186–203.

Marshall, A. G., Hendon, H. H., & Son, S.-W. (2017). Impact of the quasi-biennial

oscillation on predictability of the MaddenJulian Oscillation. *Clim. Dyn.*, *49*(4), 1365-1377. doi: https://doi.org/10.1007/s00382-016-3392-0

Mills, M. J., Richter, J. H., Tilmes, S., Kravitz, B., MacMartin, D. G., Glanville, A. A., ... Kinnison, D. E. (2017). Radiative and chemical response to interactive stratospheric sulfate aerosols in fully coupled CESM1(WACCM). *J. Geophys. Res. Atmos.*, *122*, 13,06113,078.

Podglajen, A., Plougonven, R., Hertzog, A., & Legras, B. (2016). A modelling case study of a large-scale cirrus in the tropical tropopause layer. *Atmos. Chem. Phys.*, *16*(6), 3881–3902. Retrieved from `https://www.atmos-chem-phys.net/16/3881/2016/` doi: 10.5194/acp-16-3881-2016

Richter, J. H., Anstey, J. A., Butchart, N., Kawatani, Y., et al. (2020). Progress in simulating the quasibiennial oscillation in CMIP models. *J. Geophys. Res. Atmos.*, *125*(8), e2019JD032362. doi: 10.1029/2019JD032362

Richter, J. H., Butchart, N., Kawatani, Y., Bushell, A. C., Holt, L., Serva, F., ... Yukimoto, S. (2020). Response of the quasi-biennial oscillation to a warming climate in global climate models. *Q. J. Roy. Meteorol. Soc.*, *n/a*(n/a), (in press). doi: 10.1002/qj.3749

Richter, J. H., Sassi, F., & Garcia, R. R. (2010). Towards a physically based gravity wave source parameterization. *J. Atmos. Sci.*, *67*, 136-156.

Richter, J. H., Solomon, A., & Bacmeister, J. T. (2014). On the simulation of the quasi-biennial oscillation in the Community Atmosphere Model, version 5. *J. Geophys. Res. Atmos.*, *119*, 3045–3062. doi: 10.1002/2013JD021122

Scaife, A. A., Arribas, A., Blockley, E., Brookshaw, A., Clark, R. T., Dunstone, N., ... Williams, A. (2014). Skillful long-range prediction of European and North American winters. *Geophys. Res. Lett.*, *41*(7), 2514–2519. Retrieved from `http://dx.doi.org/10.1002/2014GL059637` doi: 10.1002/2014GL059637

Schirber, S., Manzini, E., Krismer, T., & Giorgetta, M. (2015). The quasi-biennial oscillation in a warmer climate: Sensitivity to different gravity wave parameterizations. *Clim. Dyn.*, *45*(3-4), 825-836. Retrieved from `http://dx.doi.org/10.1007/s00382-014-2314-2` doi: 10.1007/s00382-014-2314-2

Shige, S., Takayabu, Y., Tao, W.-K., & Johnson, D. (2004). Spectral retrieval of latent heating profiles from TRMM PR data. Part 1: Development of a model-based algorithm. *J. Appl. Meteorol.*, *43*, 1095-1113.

Shige, S., Takayabu, Y. N., Kinda, S., Tao, W.-K., Zeng, X., Yokiyama, C., & LEcuyer, T. (2009). Spectral retrieval of latent heating profiles from TRMM PR data. Part IV: Comparisons of lookup tables from two- and three-dimensional cloud-resolving model simulations. *J. Climate*, *22*, 5577–5594. doi: 10.1175/2009JCLI2919.1.

Shige, S., Takayabu, Y. N., Tao, W.-K., & Shie, C.-L. (2007). Spectral retrieval of latent heating profiles from TRMM PR data. Part 2: Algorithm improvement and heating estimates over tropical ocean regions. *J. Appl. Meteorol. and Clim.*, *46*, 1098-1124.

Shige, S., Takayabu, Y. N., Tao, W.-K., & Shie, C.-L. (2008). Spectral retrieval of latent heating profiles from TRMM PR data. Part 3: Estimating apparent moisture sink profiles over tropical oceans. *J. Appl. Meteorol. and Clim.*, *47*, 620-640.

Smith, D. M., Scaife, A. A., Eade, R., & Knight, J. R. (2016). Seasonal to decadal prediction of the winter North Atlantic Oscillation: Emerging capability and future prospects. *Q. J. Roy. Meteorol. Soc.*, *142*(695), 611-617. Retrieved from `https://rmets.onlinelibrary.wiley.com/doi/abs/10.1002/qj.2479` doi: 10.1002/qj.2479

Takayabu, Y. N., Shige, S., Tao, W.-K., & Hirota, N. (2010). Shallow and deep latent heating modes over tropical oceans observed with TRMM PR spectral latent heating data. *J. Climate*, *23*(8), 2030-2046. doi: 10.1175/2009JCLI3110.1

683 Thompson, D. W. J., & Solomon, S. (2002). Interpretation of recent Southern Hemi-
684 sphere climate change. *Science*, *296*, 895-899.
685 Vincent, R. A., & Hertzog, A. (2014). The response of superpressure balloons to
686 gravity wave motions. *Atmos. Meas. Tech.*, *7*, 10431055. doi: 10.5194/amt-7
687 -1043-2014
688 Yoo, C., & Son, S.-W. (2016). Modulation of the boreal wintertime Madden-Julian
689 oscillation by the stratospheric quasi-biennial oscillation. *Geophys. Res. Lett.*,
690 *43*(3), 1392–1398. doi: 10.1002/2016GL067762
691 Zhang, G., & McFarlane, N. (1995). Sensitivity of climate simulations to the pa-
692 rameterization of cumulus convection in the Canadian Climate Centre general
693 circulation model. *Atmos.-Ocean*, *33*(3), 407-446.